Detection of amyloid fibrils in Parkinson's disease using plasmonic chirality

Jatish Kumar[a], Hasier Eraña[b], Elena López-Martínez[a], Nathalie Claes[c], Víctor F. Martín[d], Diego M. Solís[e], Sara Bals[c], Aitziber L. Cortajarena[a,f], Joaquín Castilla[b,f], and Luis M. Liz-Marzán[a,f,g,1]

[a]Center for Cooperative Research in Biomaterials (CIC biomaGUNE), 20014 Donostia-San Sebastian, Spain; [b]Center for Cooperative Research in Biosciences (CIC bioGUNE), 48160 Derio, Bizkaia, Spain; [c]Electron Microscopy for Materials Science (EMAT), University of Antwerp, B-2020 Antwerp, Belgium; [d]Departamento de Tecnología de los Computadores y de las Comunicaciones, University of Extremadura, 10003 Cáceres, Spain; [e]Departamento de Teoría de la Señal y Comunicaciones, University of Vigo, 36301 Vigo, Spain; [f]Ikerbasque, Basque Foundation for Science, 48013 Bilbao, Spain; and [g]Biomedical Research Networking Center on Bioengineering, Biomaterials and Nanomedicine (Ciber-BBN), 20014 Donostia-San Sebastian, Spain

Amyloid fibrils, which are closely associated with various neurodegenerative diseases, are the final products in many protein aggregation pathways. The identification of fibrils at low concentration is, therefore, pivotal in disease diagnosis and development of therapeutic strategies. We report a methodology for the specific identification of amyloid fibrils using chiroptical effects in plasmonic nanoparticles. The formation of amyloid fibrils based on α-synuclein was probed using gold nanorods, which showed no apparent interaction with monomeric proteins but effective adsorption onto fibril structures via noncovalent interactions. The amyloid structure drives a helical nanorod arrangement, resulting in intense optical activity at the surface plasmon resonance wavelengths. This sensing technique was successfully applied to human brain homogenates of patients affected by Parkinson's disease, wherein protein fibrils related to the disease were identified through chiral signals from Au nanorods in the visible and near IR, whereas healthy brain samples did not exhibit any meaningful optical activity. The technique was additionally extended to the specific detection of infectious amyloids formed by prion proteins, thereby confirming the wide potential of the technique. The intense chiral response driven by strong dipolar coupling in helical Au nanorod arrangements allowed us to detect amyloid fibrils down to nanomolar concentrations.

amyloid | Parkinson's disease | gold nanorods | nanoplasmonics | plasmonic chirality

The expansion of age-related neurodegenerative disorders associated with increased life expectancy has emerged as a topic of fundamental importance in scientific research. Many of these diseases, including Alzheimer's disease, Parkinson's disease (PD), amyotrophic lateral sclerosis, and transmissible spongiform encephalopathies, are characterized by the presence of amyloid deposits made of misfolded proteins in specific regions of the nervous system (1–3). Their increasing socioeconomic impact has boosted research on the fundamental aspects as well as on the diagnosis and treatment of these disorders (4, 5). Although the mechanisms leading to neurodegeneration are not fully understood, a conformational change of native proteins resulting in the aggregation and formation of insoluble amyloid fibrils is a hallmark of all of these diseases (6–8). Therefore, tools allowing the detection of specific forms of protein aggregation are pivotal to improve the knowledge on fundamental aspects of these neurodegenerative disorders, thereby improving diagnosis and assisting the development of therapeutic strategies (9–11). However, researchers in this field are confronted with various difficulties in the detection of protein aggregates, including (*i*) the insoluble nature of the aggregates, (*ii*) differences in conformational and misfolding patterns depending on the type of protein, and (*iii*) the diverse nature of aggregates, ranging from 2D crystals to amorphous structures, protofibrils, and fibrils (10–12). Currently used methods in the detection of protein aggregation

involve intrinsic techniques [such as UV visible, corcular dichroism (CD), vibrational CD, IR, NMR spectroscopies, and X-ray diffraction] (13–16) as well as extrinsic methods involving the addition of external probes, such as antibodies and dyes (for example, Thioflavin T and Congo red) (17–21). Intrinsic methods evaluate conformational changes in the protein, whereas extrinsic ones rely on changes in the physical properties exhibited by the external probe on binding to the aggregate.

Plasmonic nanoparticles (NPs) have been proposed as materials with great potential for biomedical applications, such as biosensing, drug delivery, or photothermal therapy (22). In related examples, gold NPs have been reported to serve as both promoters and inhibitors of protein fibrillation (23–25). We were attracted by the relatively recent but intense efforts to show the generation of optical activity in the visible and near-IR (NIR) spectral regions originating from the chiral arrangement of noble metal NPs (26–29). Similar to the differential absorption of left and right circularly polarized light in optically active chiral molecules, such as DNA and proteins, strong CD signals can be generated through coupling of plasmonic dipoles in chiral metal NP assemblies. Our group reported the strong optical activity of helically arranged Au nanorods (NRs), wherein the origin of surface plasmon CD (SP-CD) was elucidated with the help of a coupled plasmon dipole model (30, 31). While the spectral position and intensity of the chiral surface plasmon activity

Significance

This contribution reports on the application of gold nanorods to the detection of amyloids in Parkinson's and prion diseases. We found that gold nanorods show no interaction with monomeric proteins but adsorb onto helical protein fibrils. Chiral amyloid templates induce helical arrangement of nanorods, giving rise to intense optical activity at the plasmon resonance wavelengths. This report shows the use of protein fibrils as templates for chiral nanoparticle assembly and development of a biodetection technique. We show this effect on a model recombinant protein, α-synuclein (involved in Parkinson's disease), using CD, cryogenic transmission EM tomography, and theoretical simulations supporting the experimental findings. We additionally show application to identify patients with Parkinson's disease from human brain homogenates.
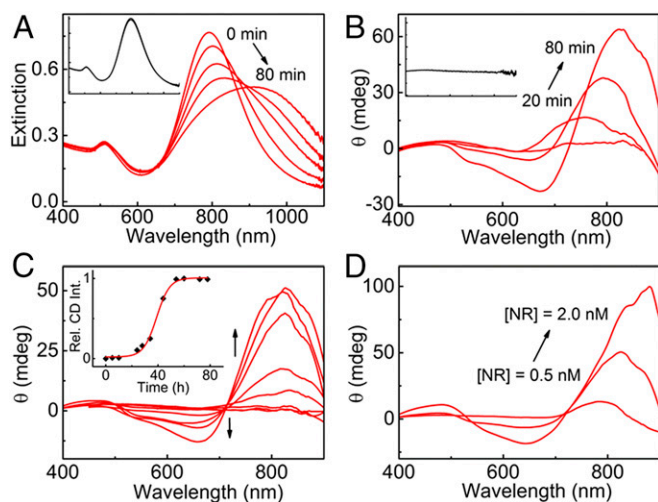
APPLIED PHYSICAL SCIENCES

Fig. 1. (*A*) Extinction and (*B*) CD spectral changes of Au NRs monitored over a time period of 80 min after the addition of α-synuclein fibrils (80 nM). Each spectrum was collected after a time interval of 20 min. *Insets* show the (absence of) spectral changes in the presence of α-synuclein monomers (1 μM). (*C*) CD spectra of different Au NR solutions after the addition of α-synuclein aliquots (80 nM) withdrawn at different times from a sample incubated in a thermoshaker at 37 °C. A plot of the normalized CD intensity vs. time is shown in *Inset*. (*D*) CD spectra of Au NR solutions of varying concentrations (0.5, 1.0, and 2.0 nM) after 80 min of the addition of α-synuclein fibrils (concentration 80 nM).

are largely dependent on the morphology of NPs and their intrinsic localized surface plasmon resonance (LSPR), the pitch and helicity of the template can also influence the chiral surface plasmon response of the composite system (32). A wide variety of chiral templates, such as organic nanostructures (30), silica (32), peptides (33, 34), and DNA (35, 36), have been reported, but interestingly, we are not aware of any report related to the use of proteins or their assemblies as chiral templates. We hypothesized that the use of protein aggregates as templates may be extremely beneficious considering that most neurodegenerative diseases are characterized by the presence of insoluble protein aggregates in the brain (1–10). We introduce in this report the use of α-synuclein amyloid fibrils (37–39) as templates for the directed assembly of metal NPs. Au NRs are not found to display a preferred interaction with monomers of α-synuclein but align helically on the amyloid fibrils resulting from α-synuclein aggregation, giving rise to well-defined chiral surface plasmons in agreement with theoretical modeling. The chiroptical response generated by these nanocomposites was used for the highly sensitive detection of amyloid fibrils both generated in vitro and extracted from brain homogenates of patients affected by PD.

Results and Discussion

Detection of α-Synuclein Fibrils. We selected α-synuclein as a model protein, which under pathological conditions, undergoes self-assembly to form aggregated structures. The aggregation pathway involves various species, such as oligomers and protofibrils, ultimately leading to the formation of amyloid fibrillar structures. We induced the aggregation of α-synuclein by incubating 100 μM purified recombinant protein in Tris·HCl buffer (pH 7.7) in a thermoshaker at 37 °C and 600 rpm for 3 d. Addition of the synuclein fibrils to a solution of spherical NPs showed a bathochromic shift in the extinction band, but feeble or no chiral signals could be registered due to weak chiral dipolar coupling (*SI Appendix*, Fig. S1). We thus explored the use of anisotropic particles, which have been reported to display enhanced optical activity due to stronger dipolar strength. Initial attempts to use Au NRs synthesized by means of the standard seed-mediated method failed first of all because of

their low colloidal stability in the buffer medium needed to handle the proteins but also because the dimensions of such NRs are too big to fit the structural features of the fibrils, which hindered their helical alignment. As a result, no noticeable changes were observed in the extinction and CD spectra on addition of the protein fibrils to the Au NR dispersion in water (*SI Appendix*, Fig. S2). We addressed this issue by synthesizing Au NRs of smaller dimensions using a modified seedless growth method (details are provided in *SI Appendix*) (40). The synthesized small NRs possessed average length of 23 nm and width of 7 nm, with a longitudinal LSPR band centered at 780 nm (*SI Appendix*, Fig. S3). Advantages of using NRs with small size include (*i*) their dimensions match well with the feature size of the nanofibrils; (*ii*) they are stable in the buffer medium where the fibrils are formed; and (*iii*) most importantly, intense chiroptical effects were observed, which allow the detection of protein aggregates at low concentration.

Biodetection studies were performed by monitoring the spectral changes resulting from the addition of α-synuclein monomers and fibrils to separate Au NR aliquots. Addition of protein monomer to the Au NR colloidal dispersion had no effect on the extinction spectrum of the plasmonic nanomaterial (Fig. 1*A*, *Inset*). The CD profile remained silent even after a 10-fold increase in protein concentration (Fig. 1*B*, *Inset*). These features are indicative of either weak protein–NR interactions or inefficient chirality transfer from the proteins to the plasmonic NPs. In contrast, addition of a small amount of protein fibrils (80 nM) to Au NRs resulted in a gradual red shift and broadening of the longitudinal plasmon band (Fig. 1*A*), and most interestingly, a bisignate CD signal was consistently observed at the longitudinal surface plasmon wavelength. The CD signal exhibited a time-dependent increase in intensity accompanied by a red shift in the peak position to the near IR region (Fig. 1*B*). While the observed extinction red shift indicates preferential tip-to-tip alignment of the NRs, the observation of SP-CD is supportive of a 3D chiral arrangement of the Au NRs dictated by the helical structure of the template (28–31). Moreover, the concomitant broadening of the band confirmed the formation of assemblies with varying sizes and orientations. We find that the chiral SP signals extend into the NIR region, and hence, the detection limit of the instrument (900 nm) may not allow us to record the complete signal. To establish the nature of chirality, experiments were performed with NRs having different LSPR. Interestingly, experiments performed using shorter NRs with longitudinal LSPR bands centered at 580 and 740 nm showed an initial negative signal (starting from higher wavelength) followed by a positive signal, with a zero cross-over coinciding with the maxima of the coupled SP band of the extinction spectrum (negative couplet). In contrast, binding of NRs with LSPR at higher wavelengths (790 and 840 nm) on protein fibrils resulted in coupled SP bands in the NIR spectral region (*SI Appendix*, Fig. S4). The CD spectrum exhibited a further red shift (above 900 nm), because of which only partial detection of the bands was possible. According to exciton (or plasmon) coupling between two equal dipoles, the degenerate excited states split into two levels. The energy of separation largely depends on the intensities and mutual distance between the dipoles. As a result of excitation into two different excited levels, a bisignate CD couplet is generated around the extinction wavelength. In this case, all experiments were carried out with NRs having LSPR at 790 nm due to higher purity of these samples and their capability to generate intense CD signals. Samples with LSPR at 730 nm or below showed weak CD due to the presence of a higher fraction of spherical particles in the sample and weaker dipole intensities of the NRs.

The optical activity of a chiral system is often quantified by using the anisotropy factor (**g** factor) given by Eq. **1**:

$$\mathbf{g} = \Delta\boldsymbol{\varepsilon}/\boldsymbol{\varepsilon}, \qquad [1]$$

where $\Delta\boldsymbol{\varepsilon}$ and $\boldsymbol{\varepsilon}$ are the molar CD and molar extinction,
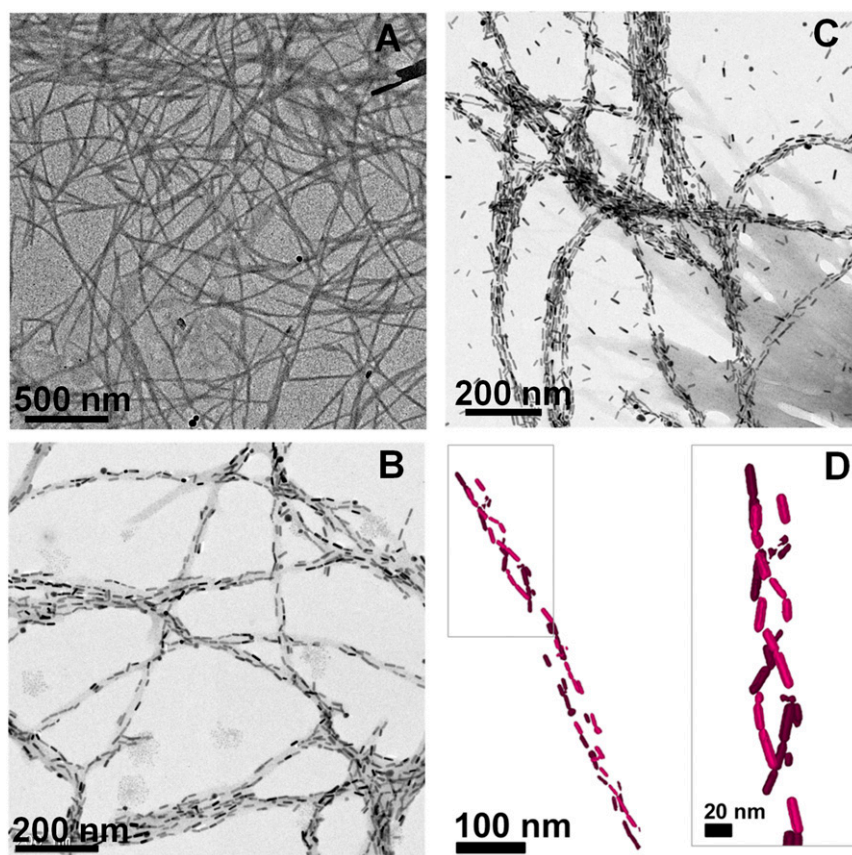
Fig. 2. (*A*) TEM images of α-synuclein fibrils. (*B* and *C*) TEM images of Au NRs in the presence of α-synuclein fibrils for varying NR concentrations: (*B*) 0.5 and (*C*) 2.0 nM. (*D*) Cryo-TEM tomography reconstruction image of a composite fiber showing the 3D chiral arrangement of Au NRs. An enlarged view of the top marked portion of the assembly is shown in *Right*. The corresponding 3D reconstructions of the 3D double-helical structure of NRs are shown in Movies S1 and S2.

respectively (41). The hybrid structures showed a remarkably high **g** factor of 0.032, which is at least one order of magnitude higher than the chiral anisotropy usually exhibited by organic molecules and dyes. The high values of chiral anisotropy displayed by Au NRs in contact with protein fibrils enabled their detection down to nanomolar concentrations. Signal reproducibility is crucial to the reliability of any detection method. We, therefore, repeated the experiments using different batches of NRs and recombinant α-synuclein fibrils. The consistently observed plasmonic CD signals and the calculated values of the anisotropy factor clearly confirmed the reproducibility of the optical CD signals (*SI Appendix*, Fig. S5). We then monitored the kinetics of protein aggregation by taking aliquots at regular time intervals from a 100 μM recombinant protein solution, incubating at 37 °C in a shaker, and adding them to separate Au NR solutions. No CD signals could be observed from aliquots extracted during the first 18 h. Weak signals appeared after 22 h, which rapidly increased in intensity during the following 40-h period. The CD signal was found to saturate at around 64 h (Fig. 1*C*). A plot of normalized CD intensity vs. incubation time resulted in a curve that is in agreement with a classical model of nucleation followed by elongation, which has been reported for α-synuclein aggregation (Fig. 1*C*, *Inset*) (14, 37). It seems evident from the profile that the aggregation process exhibits three distinct phases: (*i*) an initial lag phase before nucleation (*ii*) followed by a rapid growth phase when elongation of the fibers occurs and (*iii*) a subsequent stationary phase related to saturation of the growth process. The CD intensity was also found to be highly dependent on the concentration of Au NRs (30); an increase in SP-CD intensity was observed with increasing

concentration (Fig. 1*D*). Thus, the chiral signatures from Au NRs could be used to establish a comprehensible distinction between protein fibrils and monomers through their interaction with Au NRs in solution. The generation of chiral plasmons as a biodetection tool with no additional surface modification of either NRs or fibrils highlights the simplicity of the process.

Characterization of Nanocomposites. A direct insight into the protein–Au NR interaction was accomplished by means of EM imaging of the obtained nanocomposites. The α-synuclein nanofibers showed an average width of 9–12 nm and a length of few micrometers as determined by transmission EM (TEM) (Fig. 2*A*). TEM images from mixtures of protein monomer and Au NRs showed no specific patterns, with isolated NRs randomly distributed on the grid (*SI Appendix*, Fig. S6). Interestingly, Au NR solutions containing protein fibrils (drop casted onto a TEM grid after saturation of the absorbance and CD signals) exhibited hybrid structures with NRs arranged following the direction of the fibrils (Fig. 2 *B* and *C*). At low Au NR concentrations, TEM images show partial coverage of the fibril surface with relatively long interparticle distances (Fig. 2*B*), which is in agreement with the observed weak electromagnetic coupling and moderate SP-CD. When the concentration of NRs was increased, the surface coverage was extended, ultimately leading to saturation of the fibrils surface and additional NRs present in solution (Fig. 2*C*). As a result, strong electromagnetic coupling and intense CD signals were observed (Fig. 1*D*), in agreement with earlier studies on Au NR SP-CD (30). Careful analysis of the TEM images hinted toward a helical twist in the assembly of NRs on the fibril template (*SI Appendix*, Fig. S7), which was confirmed by carrying
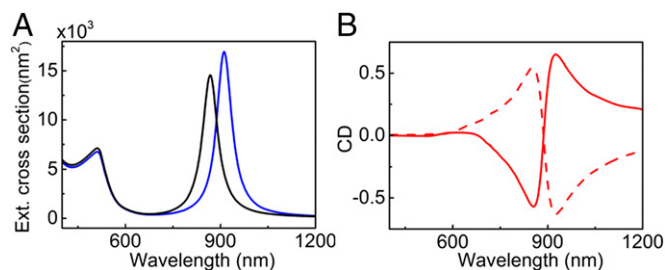
APPLIED PHYSICAL SCIENCES

Fig. 3. (*A*) Extinction spectra for an Au NR left-handed helical assembly calculated under the excitation of left- (blue trace) and right-handed (black trace) circularly polarized, axially impinging plane waves. (*B*) Simulated CD spectra for normal incidence for right- (solid curve) and left-handed (dashed curve) double helices of Au NRs (120 NRs in the helix) with interrod spacing of 4 nm.

out cryogenic transmission EM (cryo-TEM) tomography experiments (42). The electron tomography reconstructions (Fig. 2*D* and Movies S1 and S2) clearly depict a double-helix structure for the assembly of NRs with a left-handed twist. These observations corroborate the CD spectroscopy results showing intense bisignate signals at the coupled longitudinal LSPR modes with a negative couplet. As reported earlier, perfect order is not crucial toward obtaining CD signals from Au NR assemblies (30, 31). Even disordered assemblies can give rise to intense CD signals as long as the template selectively drives the arrangement of NPs in one preferred handedness. The interactions driving the adsorption of Au NRs onto the fibrils are likely to be purely electrostatic as indicated by zeta potential measurements, from which we see that Au NRs exhibit positive zeta potential values, whereas the proteins display negative surface charge (*SI Appendix*, Fig. S8). In addition, the protein shows an asymmetric distribution of acidic residues displayed mostly at the solvent exposed C terminus (*SI Appendix*, Fig. S9). We stress here that the use of Au NRs with dimensions fitting the diameter of protein fibrils facilitated the effective alignment of the NRs on the fibril surface.

Theoretical Modeling of Helical NR Assemblies. Based on the morphological characterization of the nanocomposites as well as on earlier experimental and theoretical reports, we postulated that the observed plasmon chirality originated from the 3D helical arrangement of Au NRs. We, therefore, carried out theoretical electromagnetic modeling based on advanced surface-integral equation and the method of moments combined with heuristic acceleration strategies, which allowed us to model our complex plasmonic systems (43–45). On the basis of the experimental electron tomography reconstructions, we modeled 30 different double-helix assemblies, each consisting of a sequence of 120 NRs. Extinction cross-sections for the collection of helical Au NR assemblies were calculated under the excitation of left- and right-handed circularly polarized, axially impinging plane waves (Fig. 3*A*). Both curves were then combined to calculate CD spectra, which displayed positive or negative Cotton effects for right- or left-handed double helices, respectively (Fig. 3*B*). The sign and position of the CD signal for the left-handed double helix match well with the experimental spectra (vide supra). The negative Cotton effect peak at 925 nm, which is above the saturation limit of the instrument, could not be observed in the experimental spectra. The major difference between experimental and theoretical spectra was related to the width of the CD features and the asymmetry of the bands, which is attributed to the polydispersity of the sample not accounted for in the simulations. An additional band observed below 750 nm in the experimental spectra can be ascribed to multipolar coupling or excitation through a different angle of incidence. A similar peak with weak CD was actually observed in the simulated spectra of

double-helical Au NR assemblies with oblique light incidence (*SI Appendix*, Fig. S10).

Detection of Amyloid Fibrils in Human Brain Homogenates. After we acquired experimental and theoretical demonstration of the feasibility of using chiral surface plasmons for the detection of fibrillation in recombinant α-synuclein, we extended our study to a more complex and realistic system. With the ultimate aim of developing a biodetection platform that can be used in real systems, experiments were designed using brain homogenates toward identifying the presence of protein fibrils in human brain samples. Two sets of brain samples from PD-affected patients (PD1 with Lewy bodies and PD2 with diffuse Lewy bodies) were collected and homogenized in a suitable buffer following a reported protocol (details are in *SI Appendix*) (46). Healthy brain homogenate was used as control. The major challenge regarding the use of brain samples was the presence of a large amount of biomolecules, including other proteins, which may interfere with the interaction between fibrils and Au NRs. Moreover, the concentration of fibrils in such brain homogenates is expected to be significantly lower than that in the purified recombinant samples previously analyzed. Therefore, addition of brain homogenate samples to Au NR colloids resulted in turbid suspensions as a result of light scattering from big aggregates, yielding extinction spectra with broad bands and large deviations from the baseline. Weak CD signals corresponding to coupled plasmon modes could be observed on addition of Parkinson's samples to Au NRs (*SI Appendix*, Fig. S11). We also found that, unlike in the case of recombinant monomeric protein, CD signals were also obtained from healthy controls. Although the differences in intensity of the recorded signals were sufficient to distinguish PD-affected samples (PD1) from healthy ones, any changes in the concentration or the nature of the sample could complicate the distinction. The difference in signals between the PD-affected (PD2) and healthy samples was actually less prominent when the experiments were performed using brain homogenates from a different Parkinson's sample PD2 (*SI Appendix*, Fig. S12). To overcome this problem, brain homogenates were subjected to purification to obtain cleaner samples free from soluble proteins and other biological moieties (46). When the purified samples were added to Au NRs, a clear red shift was observed in the longitudinal LSPR in the case of PD-affected brain homogenates but not from healthy controls (Fig. 4*A*). Intense bisignate CD signals with negative couplet were recorded from the PD sample (Fig. 4*B*), similar to the results with the recombinant α-synuclein samples (vide supra). Only a small red shift was observed in the extinction spectrum, and therefore, a negative CD peak could be observed well below 900 nm in this case. Moreover, the extinction maxima match with the zero cross-over in CD indicating plasmon coupling between adjacent NRs. Experiments with purified healthy controls showed only weak signals in the CD spectra (black traces in Fig. 4*B*). The reproducibility of the results was further confirmed through
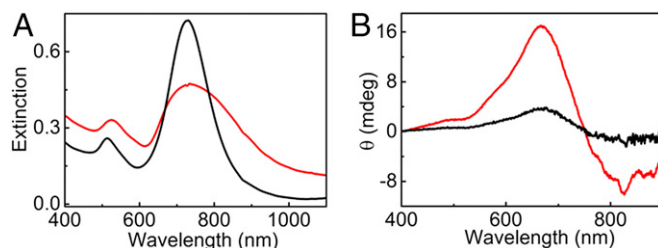

Fig. 4. (*A*) Extinction and (*B*) CD spectra of Au NRs monitored 30 min after the addition of 30 μL of purified brain homogenates from healthy (black traces) and PD-affected (red traces) patients (PD1).
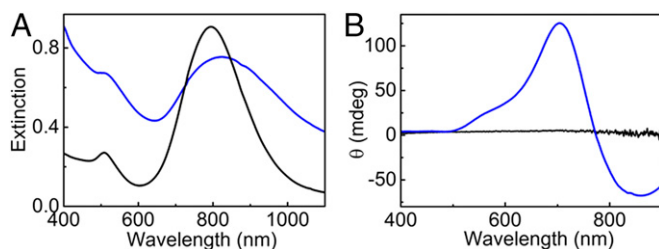
Fig. 5. (*A*) Extinction and (*B*) CD spectra of Au NRs monitored 30 min after the addition of 20 μL of native PrP (black traces) and prion fibrils (blue traces).

experiments on a different set of PD-affected brain sample (PD2) (*SI Appendix*, Fig. S13). A clear distinction was thus evident between PD-affected samples and healthy controls. The weak signals observed in the case of healthy samples are likely due to the presence of few amorphous or fibrous aggregates developed in the particular brain that was analyzed. These experiments clearly illustrate the suitability of the technique toward analysis of complex and realistic systems, such as brain homogenates.

Detection of Infectious Prion Fibrils. To further establish the wider applicability of the proposed detection technique, we additionally investigated a different protein, namely the infectious prion protein (PrP^Sc) from bank vole (*Myodes glareolus*) (47, 48). This rodent species and its particular PrP sequence present several features that make them appropriate for the investigation of prion diseases: (*i*) it develops a spontaneous prion disease, (*ii*) it gives rise to the fastest prion disorder known when infected with cervid (chronic wasting disease) prions, and (*iii*) it is considered a universal acceptor of prions due to its high susceptibility to prion infection (49–51). This recombinant bank vole PrP misfolds into infectious prion fibrils under suitable experimental conditions as recently reported, with average length of 40–60 nm and width of 15–20 nm (49). The addition of prion fibrils to Au NRs in a mixture of water and PBS-NaCl buffer resulted in extensive red shift and broadening of the longitudinal plasmon band (Fig. 5*A*, blue trace). Intense bisignate CD signals at the plasmon wavelength indicated again the helical assembly of NRs on the fibrillar surface (Fig. 5*B*, blue trace). A bisignate CD signal was observed at the longitudinal plasmon wavelength with a negative couplet. From the theoretical simulations (vide supra), we can see that the sign of the recorded CD signal is indicative of a left-handed arrangement of Au NRs on the prion fibrils. Similar experiments with native monomeric PrP resulted in no spectral changes (Fig. 5*B*, black trace), but it should be mentioned that weak CD signals were occasionally observed at the plasmon wavelength. PrP is known to form different types of aggregates from soft noninfectious amorphous structures to infectious amyloid fibrils. Purification of the samples proved that the CD signals observed in monomeric nonmisfolded protein arose from the presence of amorphous aggregates generated in solution when stored for extended periods of time (*SI Appendix*, Fig. S14). These results indicate that even amorphous aggregates in solution are capable of generating plasmonic CD due to the chiral nature of the protein and the sensitivity of NR assemblies toward asymmetry (43). However, the intensity of the CD signal seems to be largely dependent on the quality of the sample/chiral template, and therefore, fibrils with chiral 1D structure serve as better templates in terms of driving a helical assembly of Au NRs

and thereby, generating intense chiral surface plasmons. The poor electronic contrast of the fibrils in this case hindered the direct observation of NR assemblies using EM imaging. The spectroscopic data, however, fully support the hypothesis that chiral surface plasmons arise as a result of the helical assembly of Au NRs on chiral prion fibrils. Detection of aggregated proteins at nanomolar concentrations was again possible by the intense SP-CD exhibited by the hybrid structures, highlighting the efficiency of the proposed sensing technique.

Conclusions

We developed a methodology based on chiral surface plasmons for the detection of amyloids in scrambled proteins. Focusing our investigations on α-synuclein proteins, we exploited the helical nature of amyloid fibrils to drive the assembly of (small) Au NRs on their surface. A clear distinction was observed between the monomeric state and the fibrillar state of the proteins with intense plasmonic CD for fibrils and no peaks for monomers. The size of the selected NRs facilitated a proper fit onto amyloid fibrils for the electrostatic interaction between the two, thereby generating intense optical activity. Electron tomography reconstructions allowed us to confirm a 3D structure with a double-helical arrangement of Au NRs. Theoretical modeling was also found to be in good agreement with the experimental data and established that the observed optical activity arises from dipolar coupling between adjacent NRs arranged in a chiral pattern. Therefore, the intense chiroptical activity resulting from the helical NR assembly can be used for the detection of amyloid fibrils at very low (nanomolar) concentration. We further showed that this technique could be successfully expanded to the detection of one of the pathognomonic signs in PD-affected brain homogenates (α-synuclein amyloid fibrils), whereas both monomeric recombinant proteins and healthy human brain controls generated no (or weak) plasmonic chirality. Another interesting result is that the same technique could be successfully extended to the detection of infectious recombinant prions, which points toward a wide generality of the method. It should be realized that formation of amyloids is a highly complex process, where a single method cannot be expected to analyze the entire pathway of events. Therefore, a methodology that can be useful in the characterization of aggregated species is extremely important in itself. The combination of Au NRs with 3D chiral protein templates as described herein cannot only be used as a platform for amyloid detection but also, provides deeper insight into the process of template-driven plasmon chirality.

Materials and Methods

SI Appendix discusses all experimental procedures, such as synthesis of Au NRs, purification of proteins, details on cryo-TEM sample preparation, and theoretical simulations. More details are in *SI Appendix*, Figs. S1–S14. Cryo-TEM tomographic 3D reconstruction videos are also available (Movies S1 and S2).

1. Knowles TPJ, Vendruscolo M, Dobson CM (2014) The amyloid state and its association with protein misfolding diseases. *Nat Rev Mol Cell Biol* 15:384–396.
2. Ross CA, Poirier MA (2004) Protein aggregation and neurodegenerative disease. *Nat Med* 10:S10–S17.
3. Aguzzi A, Calella AM (2009) Prions: Protein aggregation and infectious diseases. *Physiol Rev* 89:1105–1152.
4. Chiti F, Dobson CM (2006) Protein misfolding, functional amyloid, and human disease. *Annu Rev Biochem* 75:333–366.

APPLIED PHYSICAL SCIENCES

5. Barnham KJ, Bush AI (2014) Biological metals and metal-targeting compounds in major neurodegenerative diseases. *Chem Soc Rev* 43:6727–6749.

6. Ke PC, et al. (2017) Implications of peptide assemblies in amyloid diseases. *Chem Soc Rev* 46:6492–6531.

7. Eichner T, Radford SE (2011) A diversity of assembly mechanisms of a generic amyloid fold. *Mol Cell* 43:8–18.

8. Fitzpatrick AWP, et al. (2013) Atomic structure and hierarchical assembly of a cross-β amyloid fibril. *Proc Natl Acad Sci USA* 110:5468–5473.

9. van Ham TJ, Breitling R, Swertz MA, Nollen EA (2009) Neurodegenerative diseases: Lessons from genome-wide screens in small model organisms. *EMBO Mol Med* 1: 360–370.

10. Miranker A, Robinson CV, Radford SE, Aplin RT, Dobson CM (1993) Detection of transient protein folding populations by mass spectrometry. *Science* 262:896–900.

11. Pedersen JT, Heegaard NHH (2013) Analysis of protein aggregation in neurodegen-erative disease. *Anal Chem* 85:4215–4227.

12. Wei G, et al. (2017) Self-assembling peptide and protein amyloids: From structure to tailored function in nanotechnology. *Chem Soc Rev* 46:4661–4708.

13. Sawaya MR, et al. (2007) Atomic structures of amyloid cross-beta spines reveal varied steric zippers. *Nature* 447:453–457.

14. Ghosh D, et al. (2015) Structure based aggregation studies reveal the presence of helix-rich intermediate during α-synuclein aggregation. *Sci Rep* 5:9228.

15. Roeters SJ, et al. (2017) Evidence for intramolecular antiparallel beta-sheet structure in alpha-synuclein fibrils from a combination of two-dimensional infrared spectros-copy and atomic force microscopy. *Sci Rep* 7:41051.

16. Ma S, et al. (2007) Vibrational circular dichroism shows unusual sensitivity to protein fibril formation and development in solution. *J Am Chem Soc* 129:12364–12365.

17. Schütz AK, et al. (2011) The amyloid-Congo red interface at atomic resolution. *Angew Chem Int Ed Engl* 50:5956–5960.

18. Nilsson KP (2009) Small organic probes as amyloid specific ligands–Past and recent molecular scaffolds. *FEBS Lett* 583:2593–2599.

19. Kumar M, Hong Y, Thorn DC, Ecroyd H, Carver JA (2017) Monitoring early-stage protein aggregation by an aggregation-induced emission fluorogen. *Anal Chem* 89: 9322–9329.

20. Wu C, et al. (2008) The binding of thioflavin T and its neutral analog BTA-1 to pro-tofibrils of the Alzheimer's disease Abeta(16-22) peptide probed by molecular dy-namics simulations. *J Mol Biol* 384:718–729.

21. Cook NP, Kilpatrick K, Segatori L, Martí AA (2012) Detection of α-synuclein amyloi-dogenic aggregates in vitro and in cells using light-switching dipyridophenazine ru-thenium(II) complexes. *J Am Chem Soc* 134:20776–20782.

22. Giner-Casares JJ, Liz-Marzán LM (2014) Plasmonic nanoparticles in 2D for biological applications: Toward active multipurpose platforms. *Nano Today* 9:365–377.

23. Fernández C, et al. (2016) Nucleation of amyloid oligomers by RepA-WH1-prionoid-functionalized gold nanorods. *Angew Chem Int Ed Engl* 55:11237–11241.

24. Sudhakar S, Santhosh PB, Mani E (2017) Dual role of gold nanorods: Inhibition and dissolution of Aβ fibrils induced by near IR laser. *ACS Chem Neurosci* 8:2325–2334.

25. Alvarez YD, et al. (2013) Influence of gold nanoparticles on the kinetics of α-synuclein aggregation. *Nano Lett* 13:6156–6163.

26. Hentschel M, Schäferling M, Duan X, Giessen H, Liu N (2017) Chiral plasmonics. *Sci Adv* 3:e1602735.

27. Ma W, et al. (2017) Chiral inorganic nanostructures. *Chem Rev* 117:8041–8093.

28. Kumar J, Thomas KG, Liz-Marzán LM (2016) Nanoscale chirality in metal and semi-conductor nanoparticles. *Chem Commun (Camb)* 52:12555–12569.

29. Valev VK, Baumberg JJ, Sibilia C, Verbiest T (2013) Chirality and chiroptical effects in plasmonic nanostructures: Fundamentals, recent progress, and outlook. *Adv Mater* 25:2517–2534.

30. Guerrero-Martínez A, et al. (2011) Intense optical activity from three-dimensional chiral ordering of plasmonic nanoantennas. *Angew Chem Int Ed Engl* 50:5499–5503.

31. Auguié B, Alonso-Gómez JL, Guerrero-Martínez A, Liz-Marzán LM (2011) Fingers crossed: Optical activity of a chiral dimer of plasmonic nanorods. *J Phys Chem Lett* 2: 846–851.

32. Cheng J, et al. (2017) GoldHelix: Gold nanoparticles forming 3D helical superstruc-tures with controlled morphology and strong chiroptical property. *ACS Nano* 11: 3806–3818.

33. Song C, et al. (2013) Tailorable plasmonic circular dichroism properties of helical nanoparticle superstructures. *Nano Lett* 13:3256–3261.

34. George J, Thomas KG (2010) Surface plasmon coupled circular dichroism of Au nanoparticles on peptide nanotubes. *J Am Chem Soc* 132:2502–2503.

35. Kuzyk A, et al. (2012) DNA-based self-assembly of chiral plasmonic nanostructures with tailored optical response. *Nature* 483:311–314.

36. Lan X, et al. (2015) Au nanorod helical superstructures with designed chirality. *J Am Chem Soc* 137:457–462.

37. Buell AK, et al. (2014) Solution conditions determine the relative importance of nu-cleation and growth processes in α-synuclein aggregation. *Proc Natl Acad Sci USA* 111: 7671–7676.

38. Lashuel HA, Overk CR, Oueslati A, Masliah E (2013) The many faces of α-synuclein: From structure and toxicity to therapeutic target. *Nat Rev Neurosci* 14:38–48.

39. Fink AL (2006) The aggregation and fibrillation of α-synuclein. *Acc Chem Res* 39: 628–634.

40. Ali MRK, Snyder B, El-Sayed MA (2012) Synthesis and optical properties of small Au nanorods using a seedless growth technique. *Langmuir* 28:9807–9815.

41. Berova N, Di Bari L, Pescitelli G (2007) Application of electronic circular dichroism in configurational and conformational analysis of organic compounds. *Chem Soc Rev* 36: 914–931.

42. Bals S, Goris B, Liz-Marzán LM, Van Tendeloo G (2014) Three-dimensional charac-terization of noble-metal nanoparticles and their assemblies by electron tomography. *Angew Chem Int Ed Engl* 53:10600–10610.

43. Solís DM, Taboada JM, Obelleiro F, Liz-Marzán LM, García de Abajo FJ (2014) Toward ultimate nanoplasmonics modeling. *ACS Nano* 8:7559–7570.

44. Taboada JM, Rivero J, Obelleiro F, Araújo MG, Landesa L (2011) Method-of-moments formulation for the analysis of plasmonic nano-optical antennas. *J Opt Soc Am A Opt Image Sci Vis* 28:1341–1348.

45. Solís DM, Taboada JM, Obelleiro F (2015) Surface integral equation method of mo-ments with multiregion basis functions applied to plasmonics. *IEEE Trans Antennas Propag* 63:2141–2152.

46. Recasens A, et al. (2014) Lewy body extracts from Parkinson disease brains trigger α-synuclein pathology and neurodegeneration in mice and monkeys. *Ann Neurol* 75: 351–362.

47. Elezgarai SR, et al. (2017) Generation of a new infectious recombinant prion: A model to understand Gerstmann-Sträussler-Scheinker syndrome. *Sci Rep* 7:9584.

48. Fernández-Borges N, et al. (2017) Cofactors influence the biological properties of infectious recombinant prions. *Acta Neuropathol* 135:179–199.

49. Watts JC, et al. (2012) Spontaneous generation of rapidly transmissible prions in transgenic mice expressing wild-type bank vole prion protein. *Proc Natl Acad Sci USA* 109:3498–3503.

50. Di Bari MA, et al. (2013) Chronic wasting disease in bank voles: Characterisation of the shortest incubation time model for prion diseases. *PLoS Pathog* 9:e1003219.

51. Watts JC, et al. (2014) Evidence that bank vole PrP is a universal acceptor for prions. *PLoS Pathog* 10:e1003990.